



In situ unraveling surface reconstruction of Ni₅P₄@FeP nanosheet array for superior alkaline oxygen evolution reaction

Ying Li^a, Yanyan Wu^{a,b}, Hongru Hao^a, Mengke Yuan^a, Zhe Lv^a, Lingling Xu^c, Bo Wei^{a,*}

^a School of Physics, Harbin Institute of Technology, 92 West Dazhi Str., Harbin, Heilongjiang 150001, China

^b College of Physics Science and Technology, Shenyang Normal University, 110034 Shenyang, China

^c Key Laboratory of Photonic and Electric Bandgap Materials, Ministry of Education, School of Physics and Electronic Engineering, Harbin Normal University, Harbin 150025, China

ARTICLE INFO

Keywords:

Electrochemical water splitting
Oxygen evolution reaction
Phosphides
In situ Raman spectroscopy
Surface reconstruction

ABSTRACT

Oxygen evolution reaction (OER) is a key step for electrochemical water splitting and understanding the surface reconstruction of OER pre-catalysts is of vital importance. Herein, hybrid Ni₅P₄@FeP nanosheet arrays were evaluated as promising OER pre-catalysts. The dynamic surface evolution was probed by *in situ* Raman spectroscopy, which revealed that Ni₅P₄@FeP was rapidly reconstructed to NiFe₂O₄ during the anodic scan. The structural instability of amorphous NiFe₂O₄ led to partial reconstitution to Ni/FeOOH at high oxidation potentials. As-formed Ni/FeOOH@NiFe₂O₄ hybrid with high structural reversibility was established as a truly active species, which exhibited excellent alkaline OER performance with a low overpotential of 205 and 242 mV under current densities of 10 and 100 mA cm⁻², respectively. This work provides a facile strategy to *in situ* construct an amorphous spinel/oxyhydroxide hybrid structure using electrochemical activation that holds strong promise for potential application in electrochemical water splitting and related energy devices.

1. Introduction

Electrochemical water splitting is generally regarded as among the most efficient methods for high-purity sustainable hydrogen production [1]. Regrettably, the bottleneck of this process is the oxygen evolution reaction (OER), where a sluggish four proton-coupled electron transfer processes are involved [2]. Because of their sluggish kinetics, high overpotential is accordingly required to drive the reaction [3,4]. Though oxides of iridium and ruthenium oxides are widely acknowledged as the most advanced OER catalysts, the low earth abundance and high cost can not support their large-scale commercialization [5,6]. Therefore, it is a top priority to develop high-efficiency and earth-rich alternatives to precious metals. The application of high-performance, non-precious metal-based OER electrocatalysts will benefit large-scale hydrogen production. Hence, substantial efforts have been devoted to exploring electrocatalysts, including transition-metal oxides, (oxy)hydroxides, spinel oxides, sulfides, phosphides, which demonstrate comparable and even better OER activity than the benchmark RuO₂ or IrO₂ in alkaline media [7–10].

Transition metal phosphides (TMPs) have received extensive attention for their good electrical conductivity and fast charge transfer [11].

For example, Ni₁₂P₅ [12], Fe₂P [13] and Ni/Ni₂P [14] have been reported for efficient OER electrocatalysts. Further improving the OER activity of TMPs can be achieved via composition design, heterostructure construction [15], defect engineering [16] or microstructure control etc [17]. Since phosphides are thermodynamically unstable in strongly oxidative environments, the surface of phosphides as pre-catalysts will undergo dynamic reconstruction with the formation of oxides or (oxy)hydroxides [18], which are essential for high OER activity [19]. Apparently, probing the surface evolution of electrocatalysts and identifying the metastable intermediate states during OER are very important to reveal the true active phases and thereby the underlying mechanisms [20]. Recently, the introduction of *in situ* tools to dynamically capture structural or compositional evolution of catalysts under operating conditions has attracted great interest [21]. For instance, with the help of *in situ* Raman technique, Hu et al. detected the formation of NiOOH layer on Ni₂P surface upon the anodic polarization and the real catalytic species is Ni₂P/NiOOH core-shell structure [22]. Cheng et al. found that Fe₂O₃@Ni₂P/Ni(PO₃)₂ transformed into amorphous NiOOH and FeOOH structures, serving as the real catalytic phases [23]. Recent studies have confirmed that bimetallic phosphides exhibit superior activity to monophosphides, therefore their surface reorganization process

* Corresponding author.

E-mail address: bowei@hit.edu.cn (B. Wei).

<https://doi.org/10.1016/j.apcatb.2021.121033>

Received 31 August 2021; Received in revised form 7 November 2021; Accepted 20 December 2021

Available online 23 December 2021

0926-3373/© 2021 Elsevier B.V. All rights reserved.

and the real OER active phases are interesting and valuable issues deserving studying.

Herein, we developed Ni_5P_4 @FeP nanosheet hybrids on Ni foam for OER pre-catalysts. Joint in situ Raman spectroscopy and *ex situ* tools were used to capture the surface evolution. Our results showed that Ni_5P_4 @FeP was rapidly reconstructed to NiFe_2O_4 and was further oxidized to amorphous $\text{Ni}/\text{FeOOH}@ \text{NiFe}_2\text{O}_4$ intermediates at high potentials, which function as the real active species toward OER. As-obtained amorphous hybrid with abundant defects demonstrated superior OER activity with a small overpotential and excellent stability, enabling Ni_5P_4 @FeP a very promising OER pre-catalyst for water splitting.

2. Experimental section

2.1. Materials

Ni foam (NF), Fe foam (IF) with a thickness of 1.5 mm (number of pores per inch: 110) were purchased from Beijing Saibo Electrochemical Material Co., Ltd. Iron (III) chloride hexahydrate ($\text{FeCl}_3 \cdot 6\text{H}_2\text{O}$), Potassium hydroxide (KOH) and sodium hypophosphite (NaH_2PO_2 , AR) were purchased from Aladdin Ltd. And all chemicals were directly used as received.

2.2. Synthesis of Ni_5P_4 @FeP nanosheets

Ni_5P_4 @FeP pre-catalysts were obtained by a two-step corrosion-phosphidation approach. Firstly, $\text{NiFe}(\text{OH})_x$ precursor was prepared by an ultra-fast corrosion method. A pre-heated aqueous solution with Fe^{3+} ions was prepared as follows: different amounts of iron (III) chloride hexahydrate (n M FeCl_3 , $n = 0.02, 0.05, 0.2, 0.5$) were dissolved in 25 mL of water, then heated at 100°C for 15 min. The as-prepared NFs were quickly immersed into pre-heated solutions for about 5 s, and a series of $\text{NiFe}(\text{OH})_x$ (n M) precursors were prepared. The resulting NFs were dried in a vacuum oven without washing. After that, the precursors were cleaned with DI water and ethanol several times and dried in an oven. In a common procedure of phosphidation, the NaH_2PO_2 precursor and $\text{NiFe}(\text{OH})_x$ (mass ratio of 4: 1) were loaded at two separate positions on the upstream and downstream sides of a quartz tube, respectively. Subsequently, the Ni_5P_4 @FeP has obtained through heating the precursors at 350°C for 60 min in N_2 (99.99%) atmosphere and then naturally cooled to ambient temperature. For comparison, the FeP and Ni_5P_4 were synthesized similarly using IF (0.2 M) and NF instead of $\text{NiFe}(\text{OH})_x$, respectively.

2.3. Materials characterizations

The sample crystal structures were measured by an X'Pert Pro MPD X-ray diffractometer (XRD) using $\text{Cu-K}\alpha$ radiation over the 2θ range of 10 – 90° . The surface morphologies of catalysts were obtained by a field emission scanning electron microscope (FE-SEM, Hitachi S-4800). High-resolution transmission electron microscopy (HE-TEM, Tecnai G2) was employed for further morphology characterization. The surface chemical states were examined of a surface by X-ray photoelectron spectroscopy (XPS, AXIS-His spectrometer) with an Al source. The standard binding energy of C1s (284.8 eV) was applied for adjustment.

2.4. Electrochemical measurements

All electrochemical tests were conducted using a typical three-electrode cell in O_2 -saturated 1 M KOH electrolyte solution (CHI 760E). The electrolyte was bubbled with oxygen for 30 min before the OER measurements. The fabricated catalysts were applied as the working electrode. In addition, Hg/HgO electrode and carbon rod were used for the reference electrode and counter electrode, respectively. All measured potentials were referred to the reversible hydrogen electrode

(RHE), according to the equation: $E_{\text{RHE}} = E_{\text{Hg}/\text{HgO}} + 0.098 + 0.0592 \text{ pH}$. Prior to the OER CV test, the catalysts were activated by cyclic voltammetry (CV) by cycling for 40 cycles at a scan rate of 50 mV s^{-1} . Moreover, the polarization curves were measured at scan rates of 5 mV s^{-1} to evaluate the catalytic OER performance. The ohmic resistances determined from electrochemical impedance spectra (EIS) were used to correct the polarization curves. The spectra were performed at 0.55 V vs. Hg/HgO from 100 kHz to 0.01 Hz and an AC potential amplitude of 5 mV . The double-layer capacitance (C_{dl}) values for prepared catalysts were obtained from the CV at various scan rates in the range of 0.2 – 0.25 V vs. Hg/HgO for OER. To evaluate long-term durability, chronopotentiometry (CP) test was employed for 12 h of continuous operation at 10 and 50 mA cm^{-2} , respectively. In addition, the 1000 CV cycles (scan rate of 100 mV s^{-1}) were between 0 and 1.05 V vs. Hg/HgO to evaluate the performance stability. The polarization curve of the catalysts was standardized according to the apparent area of the foam electrodes ($1 \times 1 \text{ cm}^2$).

2.5. In situ Raman spectroelectrochemical test

An XperRam Compact spectrometer with a 532 nm excitation laser was employed to obtain the *in situ* Raman spectra of the catalyst. The prepared catalyst (working electrode), Pt wire (counter electrode), and Ag/AgCl (3.5 M KCl , reference electrode) were inserted into a custom Teflon electrolytic cell. The potential was controlled by an electrochemical workstation as described previously, with applied potentials ranging from 0.97 to 1.57 V vs. RHE. CV scans were conducted at a sweep rate of 1 mV s^{-1} to acquire Raman spectra at different potentials.

3. Results and discussion

3.1. Preparation and characterization of Ni_5P_4 @FeP

As illustrated in Fig. 1, hierarchical hybrid Ni_5P_4 @FeP arrays were synthesized via a two-step corrosion-phosphidation approach, in which nickel foam (NF) was employed as both the Ni source and the conductive substrate (see Supporting information for detail). Silver gray NFs were immersed into a serial of heated FeCl_3 solutions (0.02 M – 0.5 M) to grow brown-yellow $\text{NiFe}(\text{OH})_x$ precursors (Step 1). Subsequently, these precursors were phosphatized at 350°C to form gray-black Ni_5P_4 @FeP hybrids (Step 2).

Typical *ex situ* Raman spectra of $\text{NiFe}(\text{OH})_x$ (0.2 M) and Ni_5P_4 @FeP (0.2 M) are shown in Fig. 2a. The Raman bands at about $307, 390, 458, 540, 581$, and 688 cm^{-1} indicate the coexistence of FeOOH [24] and NiFe LDH (layered double hydroxide) [25] phases in $\text{NiFe}(\text{OH})_x$, which is further supported by the XRD pattern in Fig S1. No observable Raman peak is detected for Ni_5P_4 @FeP (0.2 M). The crystalline structure of the catalysts is further unveiled by X-ray diffraction (XRD). Except for Ni support, all the diffraction peaks in Fig. 2b can be indexed to the phases of FeP (JCPDS card no. 78-1443) and Ni_5P_4 (JCPDS card no. 18-0883).

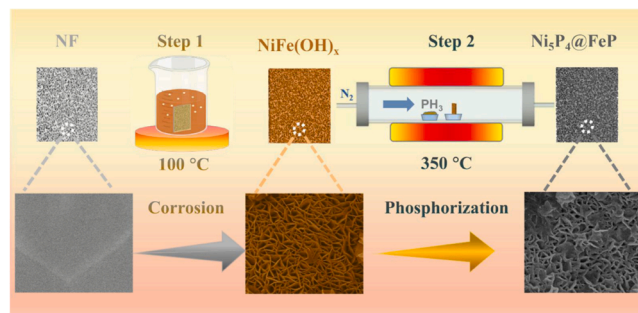


Fig. 1. Schematic illustration for the two-step synthesis of Ni_5P_4 @FeP on Ni foam through combined chemical corrosion and phosphorization method.

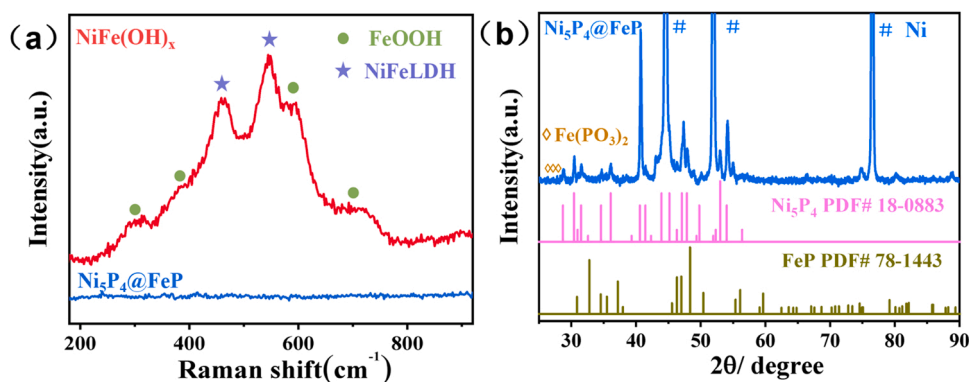


Fig. 2. (a) *Ex situ* Raman spectra of $\text{NiFe}(\text{OH})_x$ (0.2 M) and Ni_5P_4 @FeP (0.2 M) collected in air, (b) XRD pattern of Ni_5P_4 @FeP (0.2 M) on NF support.

Moreover, a small amount of $\text{Fe}(\text{PO}_3)_2$ is also detected. The XRD result reveals that complete phosphorization is achieved, with the co-formation of orthorhombic FeP and hexagonal Ni_5P_4 phases.

SEM images of $\text{NiFe}(\text{OH})_x$ (0.2 M) precursor in Fig. 3a, b reveals that the smooth nanosheets array with ample open voids is well-aligned on the Ni foam surface. Meanwhile, the TEM images also clearly show the uniform nanosheets structure (Fig. 3c). The HRTEM images in Fig. 3d, e reveal that the interplanar distances of the lattice stripes are 0.258 and 0.333 nm, assigned to the NiFe LDH (012) and FeOOH (310) planes, respectively. This can also confirm the coexistence of NiFe LDH and

FeOOH phases. The EDS spectrum confirms the coexistence of Ni, Fe, and O elements, which also proves the content with the Ni to Fe ratio close to 1:1 (Fig. 3f). The elemental mapping images (Fig. 3g) further unveil the even coverage of these elements across the nanosheets in $\text{NiFe}(\text{OH})_x$ (0.2 M).

After phosphidation, the uniform wall-like nanosheets morphology is well preserved with increased thickness and rougher surface (Fig. 4a, b). Such a highly open network enables close contact with the electrolyte, which is believed to be beneficial for mass transport during electrocatalysis. The TEM image in Fig. 4c also clearly shows that, compared to

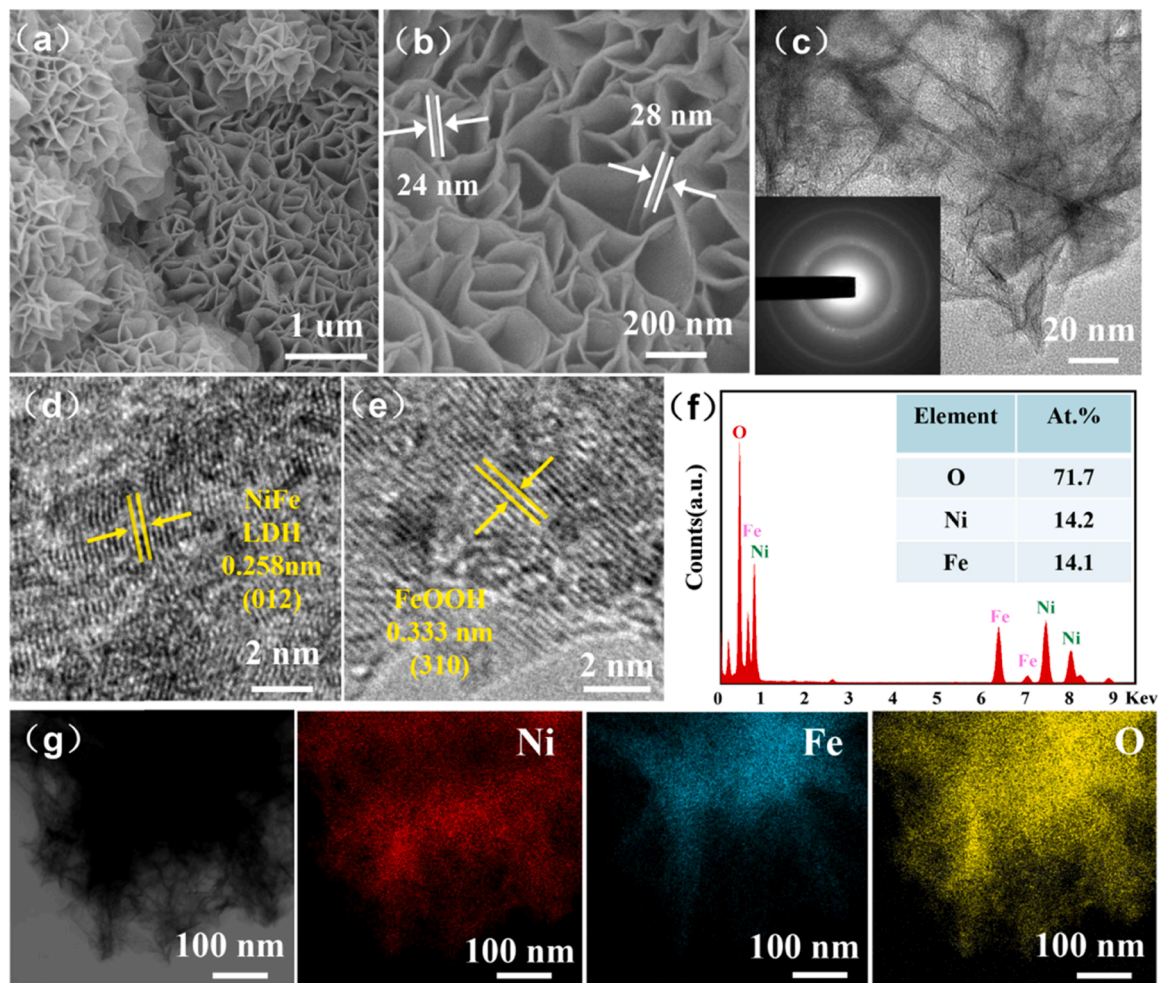


Fig. 3. (a, b) SEM image, (c) TEM image (inset: SAED pattern), (d, e) HRTEM image, (f) EDS spectra, (g) The STEM and elemental mapping images of $\text{NiFe}(\text{OH})_x$ (0.2 M) nanosheets precursor.

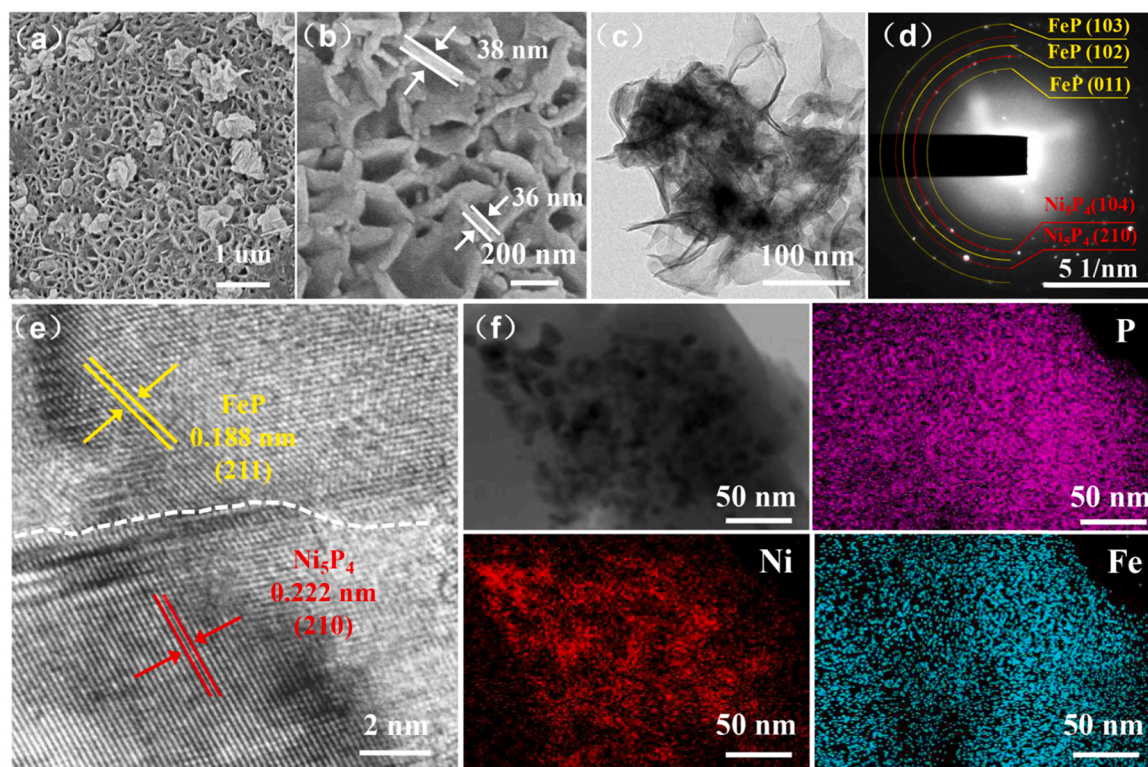


Fig. 4. (a, b) SEM image, (c) TEM image, (d) SAED pattern, (e) A typical HRTEM image, (f) The STEM and elemental mapping images of Ni_5P_4 @FeP (0.2 M) nanosheets.

the $\text{NiFe}(\text{OH})_x$ nanosheets (Fig. 3c), the surface of Ni_5P_4 @FeP becomes rougher and consists of many embedded nanocrystals (dark areas). The patterns of selected area electron diffraction (SAED) in Fig. 4d reveal the

characteristic (011), (102), and (103) facets of FeP and the (104) and (210) facets of Ni_5P_4 , respectively. The heterostructure, which can produce an interfacial bonding interaction and facilitate the exposure of

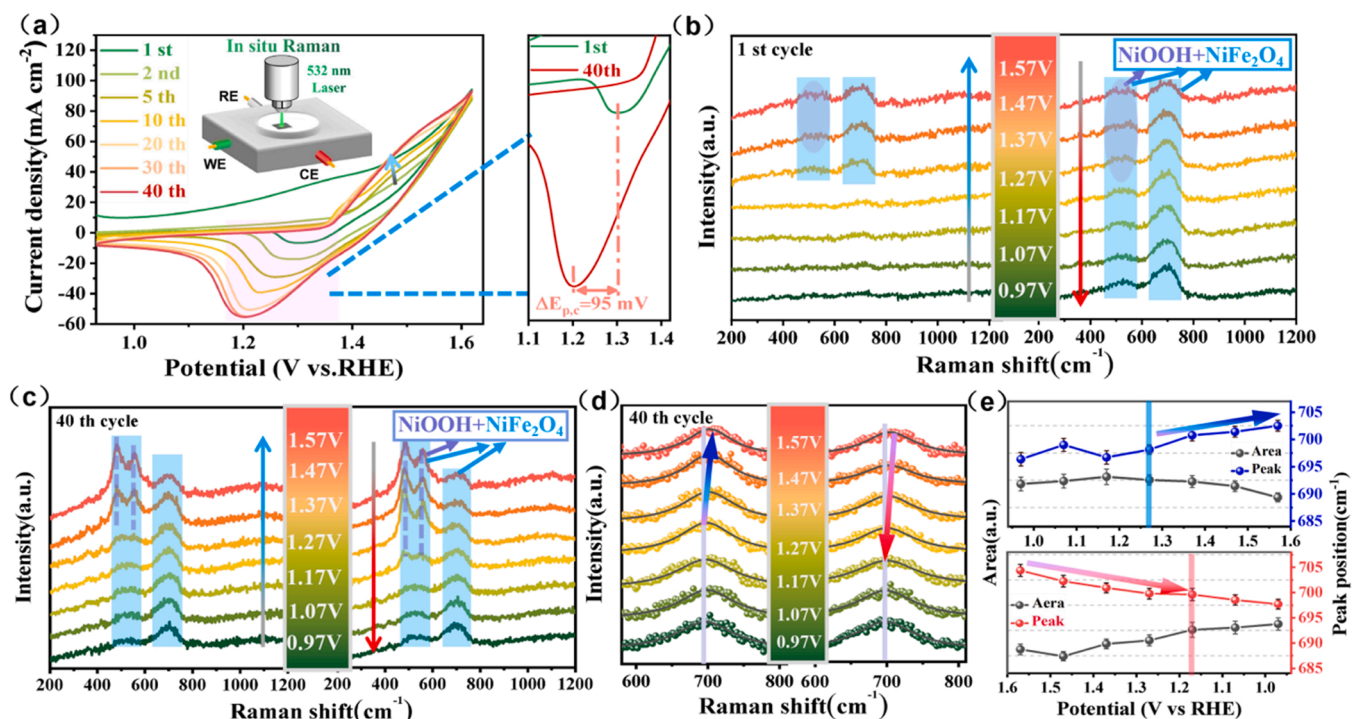


Fig. 5. (a) The evolution of CV curves for Ni_5P_4 @FeP (0.2 M), (b) *In situ* Raman spectra of Ni_5P_4 @FeP (0.2 M) pre-catalysts during the 1st CV and (c) the 40th CV, respectively, (d) enlarged view of Raman spectra for the 40th CV. The Raman A_{1g} peak of NiFe_2O_4 was fitted with Lorentzian function to extract the peak position and area (dots: raw spectra; lines: fitting results), (e) The Raman A_{1g} peak position and area plotted against the applied potential (upper panel: positive scan; lower panel: negative scan).

more active sites, can be directly observed at the Ni_5P_4 and FeP boundary, as marked in Fig. 4e. The crystalline nano-domains exhibit well-resolved lattice fringes with interplanar spacings of 0.188 and 0.222 nm, corresponding to the Ni_5P_4 (210) and FeP (211) planes, respectively. The uniform distribution of P elements across the nanosheets of Ni_5P_4 @FeP (0.2 M) was further revealed by elemental mappings (Fig. 4f). But note that the Ni element is mainly concentrated at the encapsulated nanocrystals with less Fe signal. This indicates Ni_5P_4 exists in embedded nano-domains while the FeP stays on the rest nanosheet. In addition, the same phosphorization treatment was carried out on nickel foam and iron foam (IF, 0.2 M FeCl_3) to obtain Ni_5P_4 and FeP references. The XRD patterns (Figs. S2a, S3a) and EDS profiles (Figs. S2b, S3b) confirm the successful synthesis of Ni_5P_4 and FeP electrodes. The corresponding SEM images reveal similar uniform nanosheet arrays morphology in as-prepared Ni_5P_4 (Fig. S2c–f) and FeP (Fig. S3c–f).

3.2. In situ Raman spectroscopic analysis

Prior to OER testing, 40 CV cycles were carried out in 1 M KOH to activate these pre-catalysts. The evolution of the CV curve for the Ni_5P_4 @FeP (0.2 M) electrode without iR compensation is displayed in Fig. 5a. With the increasing of cycles, the intensity of the $\text{Ni}^{2+}/\text{Ni}^{3+}$ redox peak at about 1.4 vs. RHE (reversible hydrogen electrode) gradually increases, and tends to overlap at the 30–40th scans, suggesting the pre-catalyst tends to achieve a steady-state. These redox characteristics, in turn, strongly suggest that the active phases for OER are not the as-prepared phases [26]. The growth of the Ni oxidation peak area is related to the constant formation of the electrochemically active layer on the surface of Ni_5P_4 @FeP (0.2 M) pre-catalyst, which will be discussed later. The gradual decrease in the onset potential of the nickel oxidation peak and the negative shift of the cathodic peak ($E_{p,c} = -98$ mV) indicate that the active species ($\text{Ni}^{3+}/\text{Fe}^{3+}$) is formed at a lower potential [27].

A comparison of its *ex situ* Raman spectra of Ni_5P_4 @FeP (0.2 M) before and after 40 CV scans is given in Fig. S4. The pristine one is almost Raman inactive, consistent with the previous report [28]. On the other hand, five bands centered at ~ 198 , 332, 475, 540, and 697 cm^{-1} were clearly detected after CV activation, which is assigned to the formation of inverse spinel NiFe_2O_4 [29]. In this structure, half of the Fe^{3+} cations locate at the centers of tetrahedral sites, while Ni^{2+} and the other half of Fe^{3+} occupy the octahedral sites. The strong peak at about 697 cm^{-1} is due to A_{1g} symmetry involving symmetric stretching in tetrahedral sites [30]. The rest low-frequency phonon modes are due to the involvement of metal ions in octahedral sites, i.e. E_g and T_{2g} . NiFe oxyhydroxide, which is often found in NiFe-based electrodes during OER, is not apparent in this *ex situ* collected spectrum.

To further elucidate the surface structural evolution of Ni_5P_4 @FeP (0.2 M) during OER, potential dependent in situ Raman spectroscopy was performed to comprehensively observe its progress (Figs. 5 and S5). During the first CV cycle, with the increasing of applied potential, two broad bands at $400\text{--}800\text{ cm}^{-1}$ emerge at about 1.37 V vs. RHE with gradually enhanced intensity upon positive scan (Fig. 5b). In the following negative scan, the intensity of the former band (at $450\text{--}600\text{ cm}^{-1}$) weakens, but the intensity of the latter one (at about 700 cm^{-1}) is gradually enhanced at the same time. During the following 2nd and 20th CVs, similar evolution behaviors can be observed (Fig. S5). Note that, at high overpotential region, the broad peak with increased intensity between 450 and 600 cm^{-1} separate into two bands (~ 480 and 560 cm^{-1}), which are typically determined by the E_g (bending vibration) and A_{1g} (stretching vibration) in NiOOH, respectively [31]. Additionally, the characteristic peaks of NiFe_2O_4 (~ 484 and 543 cm^{-1}) and NiOOH are partially overlapped. But they exhibit opposite potential dependences, which is more evident as indicated in the in situ Raman spectra recorded during the 40th cycle (Fig. 5c). The intensity of NiOOH predominates in the high overpotential range (1.37–1.57 V vs. RHE), while the intensity of NiFe_2O_4 becomes stronger during the

negative scan with gradual fading of NiOOH signals, indicating that NiOOH intermediate is not stable without high anodic polarization. These Raman spectroscopic results confirm the phase evolutions from phosphides to NiFe_2O_4 and NiOOH species upon CV scans.

In order to probe the changes of NiFe_2O_4 in the 40th CV cycle, the A_{1g} peak position and area were extracted by Lorentzian fitting (Fig. 5d, e). During the positive scan, when the applied potential exceeds 1.27 V vs. RHE, the A_{1g} peak produces a blue-shift with a decrease of area. While in the subsequent negative scan, a peak red-shift and increased area can be found. The shifts of Raman peaks can usually be construed as either the change in crystallinity or the resulting strain/stress (i.e., lattice contraction/extension) [32–34]. This indicates that NiFe_2O_4 starts to be oxidized at high potentials in the positive sweep, accompanied by the shortening of the M–O bond (lattice contraction) with the partial conversion of spinel to FeOOH. The reversible changes in peak position and area observed during the entire 40th CV cycle could be caused by lattice contraction/extension and surface reconstruction (Fig. 3e).

For comparison, we also conducted in situ Raman test on pure FeP and Ni_5P_4 pre-catalysts under the same conditions. For FeP, Raman spectra collected from 0.97 to 1.57 V vs. RHE (Figs. 6a and S6) reveal the generation of surface FeOOH species, as featured by two main Raman bands of 390 and 680 cm^{-1} [35]. From the Raman spectra of Ni_5P_4 (Figs. 6b and S7), it can be seen that the surface NiOOH intermediates (bands centered at 480 and 560 cm^{-1}) are formed after reconstruction. As illustrated in Fig. 6c, we directly compared the representative Raman spectra of FeP, Ni_5P_4 , and Ni_5P_4 @FeP (0.2 M) at 1.57 V vs. RHE. Two respective peaks from NiOOH in Ni_5P_4 and Ni_5P_4 @FeP (0.2 M) electrodes were fitted. The intensity ratio of the two Ni–O peaks, expressed as I_B/I_S , is closely related to the structural disorder of the NiOOH phase. The Fe doping into NiOOH can cause structural defects and lattice disorder and a lower I_B/I_S value usually indicates higher structural disorder and higher OER activity [36]. The calculated I_B/I_S value in Ni_5P_4 @FeP (1.39) is significantly lower than that in pure Ni_5P_4 (2.00). Further, the Ni–O stretching band in Ni_5P_4 @FeP ($\sim 556\text{ cm}^{-1}$) has a red-shift by about 4 cm^{-1} compared to Ni_5P_4 ($\sim 560\text{ cm}^{-1}$), which is correlated to an elongation of the Ni–O bonds caused by Fe doping [37]. In addition, the Raman evidence for the formation of FeOOH on the reconstructed Ni_5P_4 @FeP surface is not apparent. This clearly indicates that the majority of Fe element is incorporated into the NiOOH lattice, forming active Ni/FeOOH species. Based on the above analysis, we can reasonably anticipate the dynamic surface self-regeneration mechanism in Ni_5P_4 @FeP pre-catalyst, as schematically illustrated in Fig. 6d. The self-optimization process consists of the rapid oxidation of Ni/Fe phosphides (forming NiFe_2O_4 spinel) at an early stage and the fast formation of Ni/FeOOH@ NiFe_2O_4 hybrid at high overpotential range, which are considered to be active species toward OER. The potential-dependent phase transformation from NiFe_2O_4 to Ni/FeOOH@ NiFe_2O_4 hybrid is highly reversible.

3.3. Oxygen evolution reaction (OER) performance

The OER performance of foam electrodes was evaluated using a typical three-electrode cell arrangement in an oxygen saturated 1 M KOH solution. Ni_5P_4 , FeP, NF, and IF electrodes were also tested for comparison. The effect of Fe^{3+} concentration (0.02 M–0.5 M) on OER activity was first studied. As illustrated in Fig. S8, all FeCl_3 treated foams exhibit significantly higher OER performance than bare Ni_5P_4 and the optimized condition is found to be 0.2 M FeCl_3 modified sample. The OER activity parameters for the above electrodes are listed in Table S1. As also compared in Fig. 7a, the Ni_5P_4 @FeP (0.2 M) electrode demonstrates the best performance with the smallest overpotential, confirming its higher activity toward OER than the other electrodes. Specifically, it requires the lowest overpotentials of 205 and 242 mV to reach 10 and 100 mA cm^{-2} , respectively. The Ni_5P_4 @FeP (0.2 M) also exhibits the smallest Tafel slope (43.93 mV dec^{-1}) when comparing with Ni_5P_4 (84.3 mV dec^{-1}), FeP (78.2 mV dec^{-1}), IF (79 mV dec^{-1}), and NF

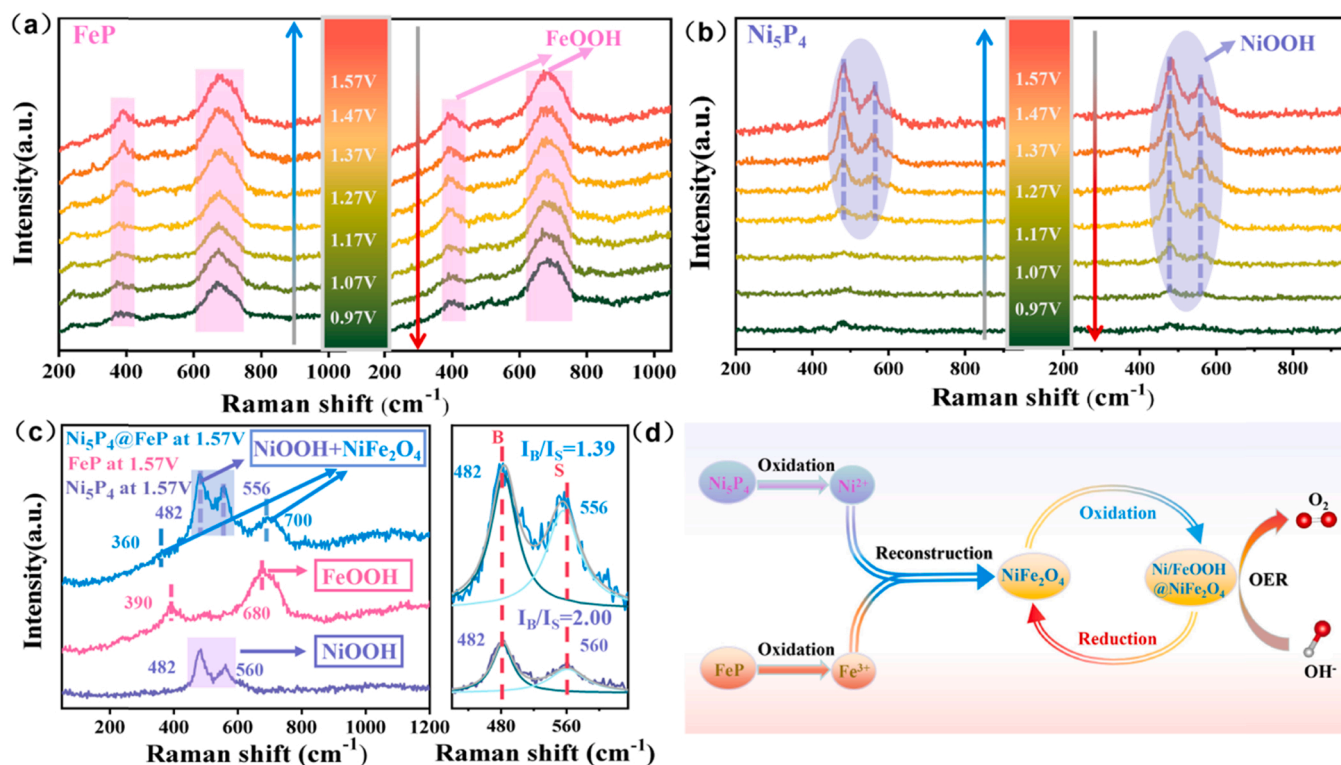


Fig. 6. *In situ* Raman spectra of (a) FeP, (b) Ni_5P_4 during the 40 th CV scan, (c) Raman spectra of Ni_5P_4 , FeP and Ni_5P_4 @FeP collected at 1.57 V vs. RHE during OER (all from the 40 th CV scan), (d) Schematic illustration of the dynamic surface reconstruction to form active of Ni/FeOOH- NiFe_2O_4 layer at the Ni_5P_4 @FeP surface.

(87.8 mV dec^{-1}), implying the superior electrocatalytic kinetics of toward OER (Fig. 7b). Electrochemical Impedance spectra (EIS) recorded at 0.55 V vs. Hg/HgO are further used to compare the electrode kinetics under OER process (Fig. 7c). In these Nyquist plots, the diameter of the semi-circle is ascribed to the charge-transfer resistance (R_{ct}) and a lower value corresponds to a quicker reaction rate. Obviously, the Ni_5P_4 @FeP (0.2 M) electrode with the highest OER activity exhibits the lowest charge-transfer resistance. To get further insight into the outstanding OER activity, the electrochemical double-layer capacitance (C_{dl}) values in Fig. 7e are utilized to compare the electrochemically active surface area (ECSA). The C_{dl} values are estimated by CV curves with different scan rates in the non-Faradic reaction range (Fig. S9). The ECSA normalized polarization curves can reflect the intrinsic activity of the catalyst. As given in Fig. 7e, the Ni_5P_4 @FeP hybrid still exhibits much better catalytic OER activity than other pre-catalysts, confirming the highest intrinsic activity in Ni_5P_4 @FeP (0.2 M). According to Raman results, it is known that FeP is reconstituted to the FeOOH phase, which however has a low intrinsic OER activity due to its poor electrical conductivity despite its high C_{dl} value [38]. To avoid the effect of Ni Foam, we used a nickel foil as a conductive substrate loaded with Ni_5P_4 @FeP powder to examine the OER performance. The relevant OER performance is provided in Fig. S10 and the above electrodes details are summarized in Table S2. As shown in Fig. S10d, the ECSA normalized LSV shows that the electrodes show close high intrinsic activity. A multi-step chronopotentiometric curve from 20 to 140 mA cm^{-2} obtained on Ni_5P_4 @FeP (0.2 M) (Fig. 7f) reflects its outstanding matter transport characteristics (the inward spreading of OH^- and outward of oxygen bubbles) and mechanical sturdiness of the Ni_5P_4 @FeP electrode. Of special note, the Ni_5P_4 @FeP (0.2 M) electrode exhibits excellent electrocatalytic OER activity and also outperforms most of the recent reported non-precious metal phosphides (Fig. 7g), such as Fe_2P , Ni_5P_4 , FeP, CoP, $(\text{Co}_{0.52}\text{Fe}_{0.48})_2\text{P}$, FeP/ Ni_2P , NiFeP, CoP-FeP and Ni_2P -CoP (details are summarized in Table S3).

3.4. OER stability and post-test characterizations

Stability is another key parameter to assess electrocatalysts, which was assessed by both multiple CV scanning and chronopotentiometric tests. Accelerated CV degeneration test was performed on Ni_5P_4 @FeP (0.2 M) by successive 1000 sweeps. *In situ* Raman spectra of Ni_5P_4 @FeP (0.2 M) during 1000th CV scan were also recorded and presented in Fig. 8a. These results illustrate similar evolution behaviors to those obtained during the 40 th CV cycle, which proves that the reconstructed Ni/FeOOH@ NiFe_2O_4 still maintains in the OER region. The *in situ* formed Ni/FeOOH and NiFe_2O_4 species are still highly reversible and they actually function as the active phases for OER. Next, the two peaks from γ -NiOOH measured at 1.57 V (1000 th) were also fitted and given in Fig. 8b. Compared to the 40th Raman spectrum (at 1.57 V), a slight decrease in peak position (from 556 to 555 cm^{-1}) and a smaller peak intensity ratio (from 1.39 to 1.35) can be found. This suggests that more Fe doping in NiOOH is achieved after 1000 continuous CV scans. The *in situ* formed Ni (oxy)hydroxide nanosheet array can provide abundant surface/defect/edge sites, which will facilitate the incorporation of Fe species. The Fe incorporation rate is much higher at OER potentials than that at the low potentials [39]. Therefore, it is reasonable that more Fe ions incorporated into the (oxy)hydroxide nanosheet during the following CV cycling, especially at high OER potential region. As given in Fig. 8c, the polarization curves are almost overlapped, demonstrating the excellent stability of Ni_5P_4 @FeP (0.2 M). A comparison of impedance spectra collected before and after the test is shown in Fig. 8d, and no significant change can be observed. Furthermore, Ni_5P_4 @FeP can catalyze the OER at both 50 and 100 mA cm^{-2} without observable decay for 50 h, further confirming its excellent durability (Fig. 8e). The above results clearly witness the robustness and outstanding OER stability of the Ni_5P_4 @FeP (0.2 M) pre-catalyst, which thus holds great promise for practical application.

After OER operation, the nanosheet array feature is well maintained in Ni_5P_4 @FeP (0.2 M) electrode (Figs. 9a, b, S11), and a close look

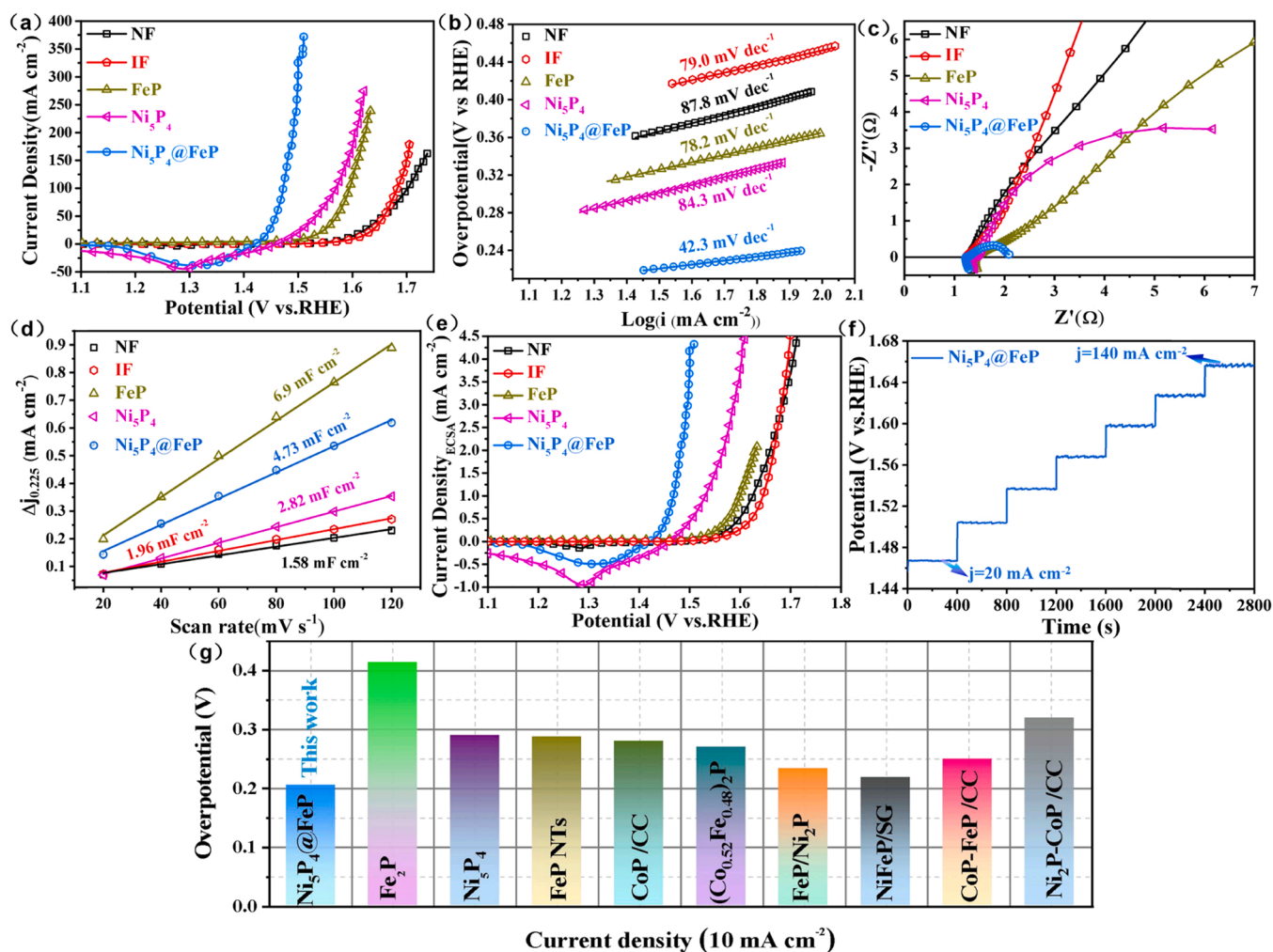


Fig. 7. A comparison of OER performance of different catalysts. (a) Polarization curves, (b) Tafel plots, (c) Electrochemical impedance spectra tested at 0.55 V vs. Hg/HgO, (d) Electrochemical double-layer capacitance, (e) Polarization curves normalized by ECSA, (f) Multi-current process of $\text{Ni}_5\text{P}_4@\text{FeP}$ (0.2 M). The test begins at 20 mA cm^{-2} to end at 140 mA cm^{-2} , which increases by 20 mA cm^{-2} per 400 s without iR-calibration, (g) Comparison of overpotentials at 10 mA cm^{-2} on various reported phosphides OER electrocatalysts.

reveals more rough surfaces with wrinkles, due to the leaching of the P element and the in situ surface reconstruction. The SAED patterns in Fig. 9c still demonstrate the characteristic (001) and (103) facets of FeP and the (002) and (104) facets of Ni_5P_4 , respectively. Moreover, halo diffraction patterns can be observed, demonstrating the existence of the amorphous structure. An HRTEM image in Fig. 9d clearly confirms the residual crystalline phosphides (region 1) in addition to the formation of considerable amorphous mater (region 2). The crystalline nano-domain displays an interplanar distance of 0.311 nm corresponding to the (103) plane of Ni_5P_4 . From the EDS profile in Fig. 9e, it is obvious that the P signal is quite weak with a significant decrease from an initial 24.99–3.54%, in agreement with the following XPS analysis. The XRD patterns before and after OER test are compared in Fig. 9f. The diffraction peaks from phosphides weaken significantly with no detection of new crystalline phases. From the residual diffraction peaks, the Ni_5P_4 is still clearly visible while FeP is quite weak. The XRD observation is consistent with the HRTEM image in Fig. 9d. The analysis of both XRD and TEM results suggests that the in situ derived NiFe_2O_4 spinel is amorphous in nature.

XPS measurement was employed to explore the surface states of pristine and $\text{Ni}_5\text{P}_4@\text{FeP}$ (0.2 M) after reconstruction. As indicated in Fig. S12, the survey spectrum of pristine one suggests the co-presence of Ni, Fe, P, and O elements, consistent with the analysis of EDS profile (Fig. S3b). For pristine one, high-resolution spectra of Ni 2p_{3/2} is shown

in Fig. 10a, which exhibits three prominent peaks, with 852.3 eV associated with Ni–P bonds, 855.6 eV (Ni^{2+}) and 856.8 eV (Ni^{3+}) assigned to Ni–O bonds and a satellite peak at 861.2 eV [40–42]. Notably, the peak of the Ni–O bond shows a negative shift ($\Delta = -0.7$ eV) after suffering OER oxidation, the Ni^{2+} species (in NiFe_2O_4) are dominant with almost vanished Ni–P bonds. Similarly, in the Fe 2p_{3/2} region (Fig. 10b), the peak at 706.7 eV corresponds to the Fe–P signal [43] becomes weaker after OER test, indicating that the apparent FeP also undergoes oxidation. Moreover, the Fe–O bonds at 711.0 and 713.6 eV [44] belonging to characteristics of Fe^{2+} and Fe^{3+} shift positively ($\Delta = 0.3$ eV), indicating that Fe was oxidized to a higher valence state during OER. The high-resolution P 2p spectra in Fig. 10c exhibit two spin-orbit doublets. The signals located at the 128.7 and 129.5 eV can be attributed to metal phosphides [45], while the rest two peaks centered at 133.5 and 134.3 eV are probably originated from surface oxidation of the phosphides in air exposure [46]. Similar to Ni–P and Fe–P bonds, the signals of P weaken significantly after the OER test, further confirming the substantial P leaching. The O 1s curves involve three peaks: O1 (530.2 eV), O2 (531.2 eV), and O3 (532.8 eV) in Fig. 10d [47–49]. Commonly, the above peaks are attributed to lattice oxygen (surface oxidized metal phosphide, O1), defect oxygen and hydroxyl groups (O2), and physically/chemical adsorbed water (O3), respectively. The ratio of O2/O1 can be a yardstick to evaluate the relative amount of surface oxygen vacancies, with a higher ratio indicating a greater

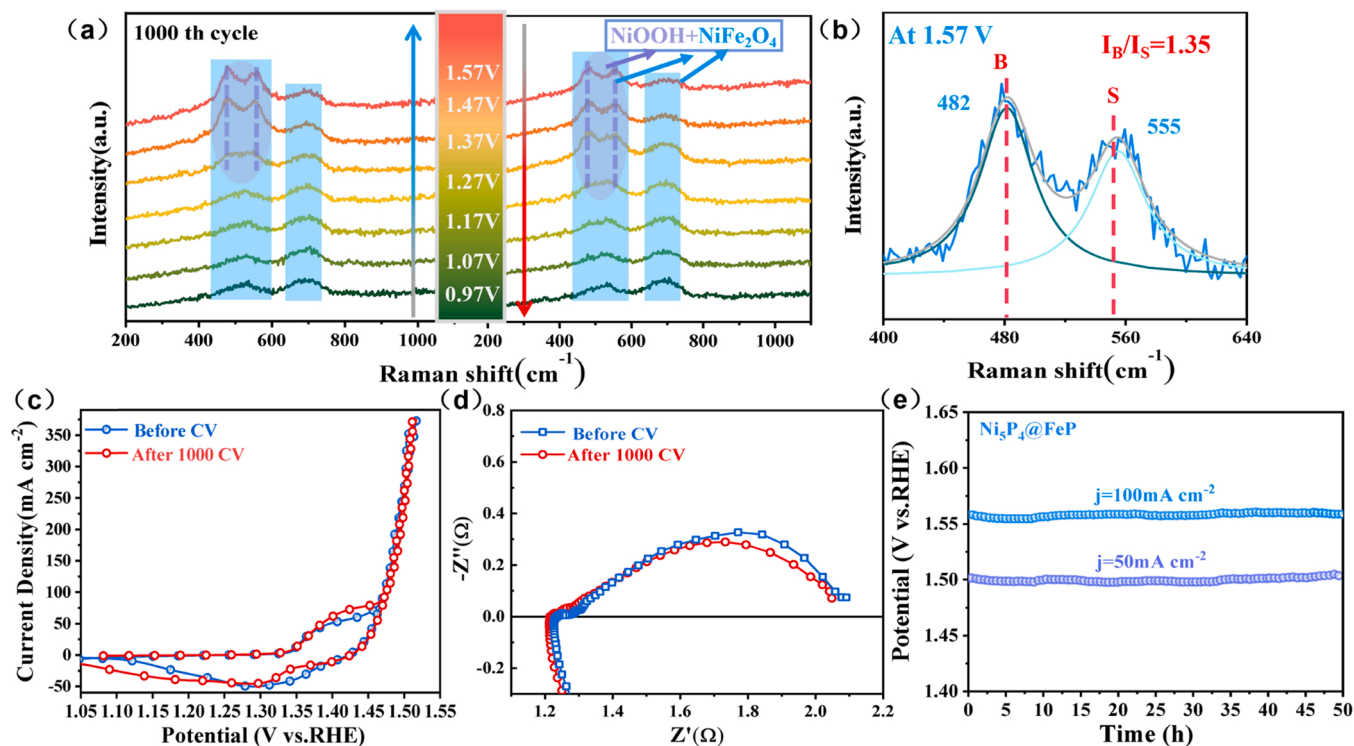


Fig. 8. (a) *In situ* Raman spectra of Ni_5P_4 @FeP (0.2 M) measured in the 1000th CV, (b) The Raman spectrum at 1.57 V was fitted to extract the peak positions and intensity ratio, (c) Polarization curves, (d) Electrochemical impedance spectra of Ni_5P_4 @FeP (0.2 M) before and after 1000 CV scans, (e) Long-term durability of Ni_5P_4 @FeP (0.2 M) operating at constant current densities of 50 and 100 mA cm^{-2} for 50 h.

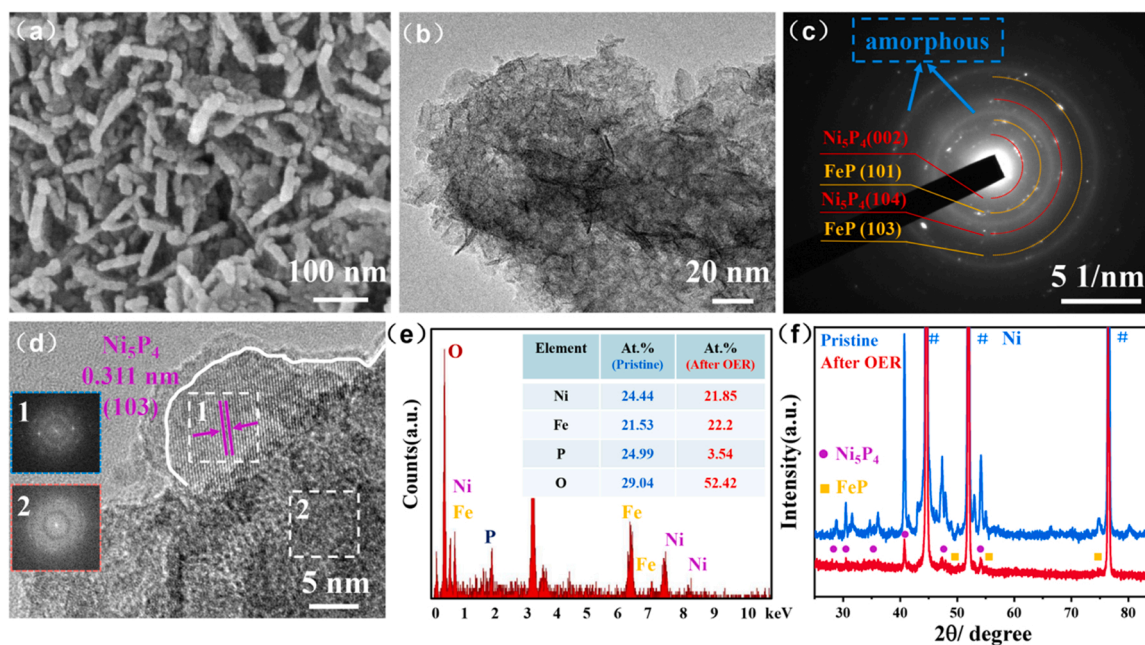


Fig. 9. Morphology and structure characterizations of Ni_5P_4 @FeP (0.2 M) after stability test. (a) SEM image, (b) TEM image, (c) SAED pattern, (d) HRTEM image, (e) EDS profile, (f) XRD patterns.

amount of surface oxygen vacancies [50]. Apparently, more oxygen vacancies ($\text{O}_2/\text{O}_1 = 8.6$) were generated on the surface of the sample after OER testing compared to the pristine ($\text{O}_2/\text{O}_1 = 5.1$), which can be attributed to the considerable defects generated in amorphous $\text{Ni}/\text{FeOOH}@\text{NiFe}_2\text{O}_4$. From the XPS findings, we can summarize that the surfaces of metal phosphides (Ni_5P_4 @FeP) have been re-arranged and oxidized with substantial P leaching during OER.

All the above results clearly indicate that the as-prepared Ni_5P_4 @FeP (0.2 M) hybrid functions as a pre-catalyst, which undergoes remarkable surface regeneration, accompanied by a considerable amount of P leaching. As determined by *operando* Raman results, the majority of phosphides are initially oxidized to NiFe_2O_4 spinel, which can be further oxidized and reconstructed to Ni/FeOOH species at higher overpotential regions. Therefore, spinel-oxyhydroxide hybrids

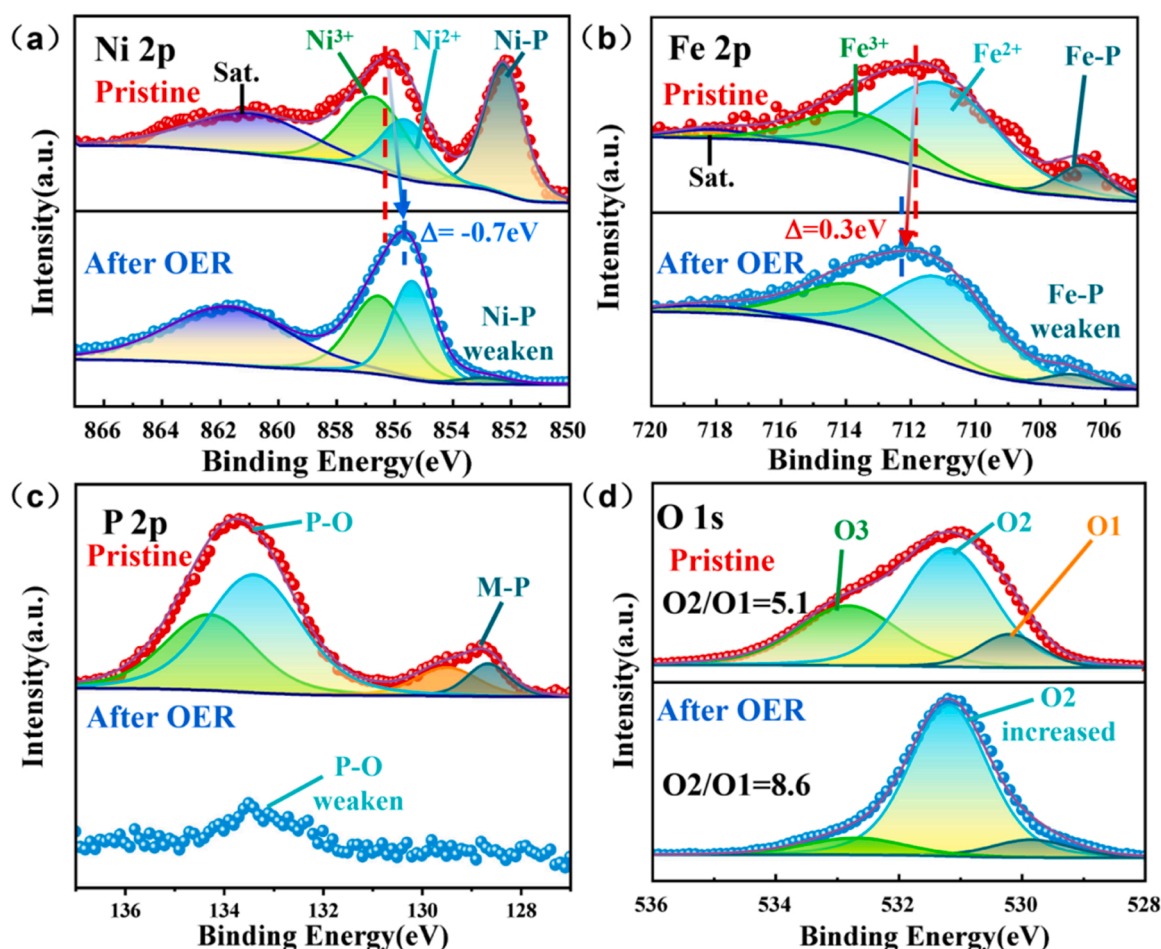


Fig. 10. High resolution XPS spectra of pristine Ni_5P_4 @FeP (0.2 M) and after OER test (a) Ni 2p, (b) Fe 2p, (c) P 2p, and (d) O 1s.

are reasonably considered as real reactive species in the OER process. The excellent performance of $\text{Ni}/\text{FeOOH}@/\text{NiFe}_2\text{O}_4$ can be mechanistically understood from the following reasons. (1) Ni/FeOOH and NiFe_2O_4 are both well-known OER catalysts with high activity, especially for the benchmark Ni/FeOOH . Simultaneous Fe doping in NiOOH and possible synergistic effect between Ni/FeOOH intermediate and amorphous NiFe_2O_4 is thought to greatly promote the OER process. (2) As-formed amorphous $\text{Ni}/\text{FeOOH}@/\text{NiFe}_2\text{O}_4$ hybrid nanosheet with highly disordered structure can provide abundant defects and interfaces between NiOOH and NiFe_2O_4 , facilitating the adsorption and desorption of surface intermediates [51]. (3) The nanosheet array with open macropores leads to easy electrolyte transportation and gas release, while the direct contact between the nanosheet electrode and the 3D metallic NF is beneficial for electron conduction.

Without the assistance of NiFe_2O_4 , on the other hand, only NiOOH exhibits quite weak activity (Fig. 7). Using Raman spectroscopy, Huang et al. probed the interfacial reaction between $\text{Ni}(\text{OH})_2$ and $\beta\text{-FeOOH}$ under electro-activation treatment, which found that the in situ formed NiFe_2O_4 contributed to improved OER activity [52]. Similarly, by direct anodization of $\text{Fe}_2\text{O}_3\text{-Ni}(\text{OH})_2$ precursor, Zhang et al. constructed amorphous $\text{NiFe}_2\text{O}_4\text{-NiOOH}$ with excellent OER activity. The strong electron donation from Fe_2O_3 to $\text{Ni}(\text{OH})_2$ leads to easier oxidation $\text{Ni}(\text{OH})_2$ to NiOOH , suggesting the crucial role of Fe ions in improving the OER activity of nickel oxide/hydroxides [53]. Compared with above two pre-catalysts, the Ni_5P_4 @FeP hybrid electrode undergoes remarkable surface regeneration, accompanied by a considerable P leaching that favors the formation of amorphous NiFe_2O_4 with abundant defects. The real active phases for OER are determined to be $\text{Ni}/\text{FeOOH}@/\text{NiFe}_2\text{O}_4$, which exhibits superior activity to the above two regenerated NiFe_2O_4

based electrodes (Table S3).

4. Conclusions

In summary, Ni_5P_4 @FeP nanosheet arrays on NF were synthesized via a two-step corrosion-phosphidation method for efficient OER pre-catalysts. Combined in situ Raman spectroscopy and *ex situ* characterizations, the surface adaptive reconstruction on Ni_5P_4 @FeP hybrid was captured and analyzed in detail. Under electrochemical scans, the surface of the pre-catalyst was rapidly oxidized to NiFe_2O_4 , which can be further partially reconstituted to Ni/FeOOH at high potentials. The reconstructed amorphous $\text{Ni}/\text{FeOOH}@/\text{NiFe}_2\text{O}_4$ composite was recognized as the real OER active phase. Moreover, in situ Raman spectra during 1000 th CV scan revealed the remarkable structural reversibility between NiFe_2O_4 and $\text{Ni}/\text{FeOOH}@/\text{NiFe}_2\text{O}_4$. As-formed amorphous hybrid with highly disordered structure and plentiful interfaces between NiOOH and NiFe_2O_4 synergistically contributed to superior alkaline OER activity. This study reveals the dynamic structural transformation of hybrid phosphides pre-catalyst in realistic conditions and the activated catalyst with excellent activity and stability holds great promise for potential application in electrochemical water splitting and related energy devices.

CRediT authorship contribution statement

Ying Li: Conceptualization, Methodology, Investigation, Writing – original draft. **Yanyan Wu:** Formal analysis, Data curation. **Hongru Hao:** Data curation, Formal analysis. **Mengke Yuan:** Data curation, Formal analysis. **Zhe Lv:** Conceptualization, Methodology. **Lingling Xu:**

Conceptualization, Methodology, Formal analysis. **Bo Wei:** Funding acquisition, Supervision, Formal analysis, Writing – review & editing.

Declaration of Competing Interest

The authors declare that they have no known competing financial interests or personal relationships that could have appeared to influence the work reported in this paper.

Acknowledgments

This work was supported by the National Natural Science Foundation of China (21773048), Natural Science Foundation of Heilongjiang Province (LH2021A013) and Sichuan Science and Technology Program (2021YFSY0022). The authors would like to thank Shiyanjia Lab (www.shiyanjia.com) for the support of XPS and TEM test.

Appendix A. Supplementary material

Supplementary data associated with this article can be found in the online version at [doi:10.1016/j.apcatb.2021.121033](https://doi.org/10.1016/j.apcatb.2021.121033).

References

- [1] Y. Jiao, Y. Zheng, M. Jaroniec, S.Z. Qiao, Design of electrocatalysts for oxygen-and hydrogen-involving energy conversion reactions, *Chem. Soc. Rev.* 44 (2015) 2060–2086.
- [2] N. Suen, S. Hung, Q. Quan, N. Zhang, Y. Xu, H.M. Chen, Electrocatalysis for the oxygen evolution reaction: recent development and future perspectives, *Chem. Soc. Rev.* 46 (2017) 337–365.
- [3] C. Wei, R.R. Rao, J. Peng, B. Huang, I.E.L. Stephens, M. Risch, Z.J. Xu, Y. Shao Horn, Recommended practices and benchmark activity for hydrogen and oxygen electrocatalysis in water splitting and fuel cells, *Adv. Mater.* 31 (2019), 1806296.
- [4] Z.Y. Yu, Y. Duan, X.Y. Feng, X. Yu, M.R. Gao, S.H. Yu, Clean and affordable hydrogen fuel from alkaline water splitting: past, recent progress, and future prospects, *Adv. Mater.* 33 (2021), 2007100.
- [5] T. Reier, M. Oezaslan, P. Strasser, Electrocatalytic oxygen evolution reaction (OER) on Ru, Ir, and Pt catalysts: a comparative study of nanoparticles and bulk materials, *ACS Catal.* 2 (2012) 1765–1772.
- [6] B. Tang, X. Yang, Z. Kang, L. Feng, Crystallized RuTe₂ as unexpected bifunctional catalyst for overall water splitting, *Appl. Catal. B Environ.* 278 (2020), 119281.
- [7] H. Liu, X. Xu, H. Xu, S. Wang, Z. Niu, Q. Jia, L. Yang, R. Cao, L. Zheng, D. Cao, Dual active site tandem catalysis of metal hydroxyl oxides and single atoms for boosting oxygen evolution reaction, *Appl. Catal. B Environ.* 297 (2021), 120451.
- [8] A. Saad, D. Liu, Y. Wu, Z. Song, Y. Li, T. Najam, K. Zong, P. Tsiakaras, X. Cai, Ag nanoparticles modified crumpled borophene supported Co₃O₄ catalyst showing superior oxygen evolution reaction (OER) performance, *Appl. Catal. B Environ.* 298 (2021), 120529.
- [9] Y.Y. Wu, Z.J. Xie, Y. Li, Z. Lü, L. Xu, B. Wei, In situ self-reconstruction of NiFeAl hybrid phosphides nanosheet arrays enables efficient oxygen evolution in alkaline, *Int. J. Hydrog. Energy* 46 (2021) 25070–25080.
- [10] L. Wu, L. Yu, F. Zhang, B. McElhenny, D. Luo, A. Karim, S. Chen, Z. Ren, Heterogeneous bimetallic phosphide Ni₂P-Fe₂P as an efficient bifunctional catalyst for water/seawater splitting, *Adv. Funct. Mater.* 31 (2021), 2006484.
- [11] Y. Shi, M. Li, Y. Yu, B. Zhang, Recent advances in nanostructured transition metal phosphides: synthesis and energy-related applications, *Energy Environ. Sci.* 13 (2020) 4564–4582.
- [12] P.W. Menezes, A. Indra, C. Das, C. Walter, C. Göbel, V. Gutkin, D. Schmeißer, M. Driess, Uncovering the nature of active species of nickel phosphide catalysts in high-performance electrochemical overall water splitting, *ACS Catal.* 7 (2017) 103–109.
- [13] Z. Pu, C. Zhang, I.S. Amiinu, W. Li, L. Wu, S. Mu, General strategy for the synthesis of transition-metal phosphide/N-doped carbon frameworks for hydrogen and oxygen evolution, *ACS Appl. Mater. Interfaces* 9 (2017) 16187–16193.
- [14] X. Li, J. Zhou, C. Liu, L. Xu, C. Lu, J. Yang, H. Pang, W. Hou, Encapsulation of Janus-structured Ni/Ni₂P nanoparticles within hierarchical wrinkled N-doped carbon nanofibers: Interface engineering induces high-efficiency water oxidation, *Appl. Catal. B Environ.* 298 (2021), 120578.
- [15] Y. Feng, C. Xu, E. Hu, B. Xia, J. Ning, C. Zheng, Y. Zhong, Z. Zhang, Y. Hu, Construction of hierarchical FeP/Ni₂P hollow nanospindles for efficient oxygen evolution, *J. Mater. Chem. A* 6 (2018) 14103–14111.
- [16] X. Zhou, H. Gao, Y. Wang, Z. Liu, J. Lin, Y. Ding, P vacancies-enriched 3D hierarchical reduced cobalt phosphide as a precursor template for defect engineering for efficient water oxidation, *J. Mater. Chem. A* 6 (2018) 14939–14948.
- [17] D. Zhao, K. Sun, W.C. Cheong, L. Zheng, C. Zhang, S. Liu, X. Cao, K. Wu, Y. Pan, Z. Zhuang, B. Hu, D. Wang, Q. Peng, C. Chen, Y. Li, Synergistically interactive pyridinic-N-MoP sites: identified active centers for enhanced hydrogen evolution in alkaline Solution, *Angew. Chem. Int. Ed.* 59 (2020) 8982–8990.
- [18] Z. Kou, X. Li, L. Zhang, W. Zang, X. Gao, J. Wang, Dynamic surface chemistry of catalysts in oxygen evolution reaction, *Small Sci.* 1 (2021), 2100011.
- [19] G. Yuan, J. Bai, L. Zhang, X. Chen, L. Ren, The effect of P vacancies on the activity of cobalt phosphide nanorods as oxygen evolution electrocatalyst in alkali, *Appl. Catal. B Environ.* 284 (2021), 119693.
- [20] J. Huang, Y. Li, Y. Zhang, G. Rao, C. Wu, Y. Hu, X. Wang, R. Lu, Y. Li, J. Xiong, Identification of key reversible intermediates in self-reconstructed nickel-based hybrid electrocatalysts for oxygen evolution, *Angew. Chem. Int. Ed.* 58 (2019) 17458–17464.
- [21] J.M. Yoo, H. Shin, S. Park, Y. Sung, Recent progress in in situ/operando analysis tools for oxygen electrocatalysis, *J. Phys. D Appl. Phys.* 54 (2021), 173001.
- [22] L. Stern, L. Feng, F. Song, X. Hu, Ni₂P as a Janus catalyst for water splitting: the oxygen evolution activity of Ni₂P nanoparticles, *Energy Environ. Sci.* 8 (2015) 2347–2351.
- [23] X. Cheng, Z. Pan, C. Lei, Y. Jin, B. Yang, Z. Li, X. Zhang, L. Lei, C. Yuan, Y. Hou, A strongly coupled 3D ternary Fe₂O₃@Ni₂P/Ni(PO₃)₂ hybrid for enhanced electrocatalytic oxygen evolution at ultra-high current densities, *J. Mater. Chem. A* 7 (2019) 965–971.
- [24] F. Froment, A. Tournié, P. Colomban, Raman identification of natural red to yellow pigments: ochre and iron-containing ores, *J. Raman Spectrosc.* 39 (2008) 560–568.
- [25] M.W. Louie, A.T. Bell, An investigation of thin-film Ni-Fe oxide catalysts for the electrochemical evolution of oxygen, *J. Am. Chem. Soc.* 135 (2013) 12329–12337.
- [26] F. Dionigi, Z. Zeng, I. Sinev, T. Merzdorf, P. Strasser, In-situ structure and catalytic mechanism of NiFe and CoFe layered double hydroxides during oxygen evolution, *Nat. Commun.* 11 (2020) 2522.
- [27] S. Li, Z. Li, R. Ma, C. Gao, L. Liu, L. Hu, J. Zhu, T. Sun, Y. Tang, D. Liu, J. Wang, A glass-ceramic with accelerated surface reconstruction toward the efficient oxygen evolution reaction, *Angew. Chem. Int. Ed.* 60 (2021) 3773–3780.
- [28] P. Yan, Q. Liu, H. Zhang, L. Qiu, H.B. Wu, X. Yu, Deeply reconstructed hierarchical and defective NiOOH/FeOOH nanoboxes with accelerated kinetics for the oxygen evolution reaction, *J. Mater. Chem. A* 9 (2021) 15586–15594.
- [29] A. Ahlawat, V.G. Sathe, Raman study of NiFe₂O₄ nanoparticles, bulk and films: effect of laser power, *J. Raman Spectrosc.* 42 (2011) 1087–1094.
- [30] P. Sivakumar, R. Ramesh, A. Ramanand, S. Ponnusamy, C. Muthamizhchelvan, Preparation and properties of nickel ferrite (NiFe₂O₄) nanoparticles via sol-gel auto-combustion method, *Mater. Res. Bull.* 46 (2011) 2204–2207.
- [31] S. Lee, K. Banjac, M. Lingenfelder, X. Hu, Oxygen isotope labeling experiments reveal different reaction sites for the oxygen evolution reaction on nickel and nickel iron oxides, *Angew. Chem. Int. Ed.* 58 (2019) 10295–10299.
- [32] B.S. Yeo, A.T. Bell, Enhanced activity of gold-supported cobalt oxide for the electrochemical evolution of oxygen, *J. Am. Chem. Soc.* 133 (2011) 5587–5593.
- [33] D. Chen, X. Xiong, B. Zhao, M.A. Mahmoud, M.A. El-Sayed, M. Liu, Probing structural evolution and charge storage mechanism of NiO₂H_x electrode materials using in operando resonance Raman spectroscopy, *Adv. Sci.* 3 (2016), 1500433.
- [34] M.W. Iqbal, K. Shahzad, R. Akbar, G. Hussain, A review on Raman finger prints of doping and strain effect in TMDs, *Microelectron. Eng.* 219 (2020), 111152.
- [35] P. Colomban, S. Cherifi, G. Despert, Raman identification of corrosion products on automotive galvanized steel sheets, *J. Raman Spectrosc.* 39 (2008) 881–886.
- [36] S. Lee, L. Bai, X. Hu, Deciphering iron-dependent activity in oxygen evolution catalyzed by nickel–iron layered double hydroxide, *Angew. Chem. Int. Ed.* 59 (2020) 8072–8077.
- [37] S. Klaus, Y. Cai, M.W. Louie, L. Trotochaud, A.T. Bell, Effects of Fe electrolyte impurities on Ni(OH)₂/NiOOH structure and oxygen evolution activity, *J. Phys. Chem. C* 119 (2015) 7243–7254.
- [38] J. Feng, H. Xu, Y. Dong, S. Ye, Y. Tong, G. Li, FeOOH/Co/FeOOH hybrid nanotube arrays as high-performance electrocatalysts for the oxygen evolution reaction, *Angew. Chem. Int. Ed.* 55 (2016) 3694–3698.
- [39] C. Kuai, C. Xi, A. Hu, Y. Zhang, Z. Xu, D. Nordlund, C. Sun, C.A. Cadigan, R. M. Richards, L. Li, C. Dong, X. Du, F. Lin, Revealing the dynamics and roles of iron incorporation in nickel hydroxide water oxidation catalysts, *J. Am. Chem. Soc.* (2021), <https://doi.org/10.1021/jacs.1c07975> (accepted).
- [40] Z. Wang, Z. Qi, X. Fan, D.Y.C. Leung, J. Long, Z. Zhang, T. Miao, S. Meng, S. Chen, X. Fu, Intimately contacted Ni₂P on CdS nanorods for highly efficient photocatalytic H₂ evolution: new phosphidation route and the interfacial separation mechanism of charge carriers, *Appl. Catal. B Environ.* 281 (2021), 119443.
- [41] Y. Wu, Y. Li, M. Yuan, H. Hao, X. San, Z. Lv, L. Xu, B. Wei, Operando capturing of surface self-reconstruction of Ni₃S₂/FeNi₂S₄ hybrid nanosheet array for overall water splitting, *Chem. Eng. J.* 427 (2022), 131944.
- [42] H. Chen, Y. Hou, Z. Wu, P. Du, L. Luo, W. Li, Simultaneous enhancement of discharge energy density and efficiency in the PMMA and PVDF blend films via introducing the Ni(OH)₂ nanosheets, *J. Alloy. Compd.* 862 (2021), 158688.
- [43] Y. Deng, Z. Xiao, Z. Wang, J. Lai, X. Liu, D. Zhang, Y. Han, S. Li, W. Sun, L. Wang, The rational adjusting of proton-feeding by Pt-doped FeP/C hollow nanorod for promoting nitrogen reduction kinetics, *Appl. Catal. B Environ.* 291 (2021), 120047.
- [44] H. Liang, C. Xia, A. Emwas, D.H. Anjum, X. Miao, H.N. Alshareef, Phosphine plasma activation of α-Fe₂O₃ for high energy asymmetric supercapacitors, *Nano Energy* 49 (2018) 155–162.
- [45] D. Liu, T. Liu, L. Zhang, F. Qu, G. Du, A.M. Asiri, X. Sun, High-performance urea electrolysis towards less energy-intensive electrochemical hydrogen production using a bifunctional catalyst electrode, *J. Mater. Chem. A* 5 (2017) 3208–3213.
- [46] F. Yu, H. Zhou, Y. Huang, J. Sun, F. Qin, J. Bao, W.A. Goddard, S. Chen, Z. Ren, High-performance bifunctional porous non-noble metal phosphide catalyst for overall water splitting, *Nat. Commun.* 9 (2018) 2551.

- [47] S. Sepulveda-Guzman, B. Rejea-Jayan, E. de la Rosa, A. Torres-Castro, V. Gonzalez-Gonzalez, M. Jose-Yacamán, Synthesis of assembled ZnO structures by precipitation method in aqueous media, *Mater. Chem. Phys.* 115 (2009) 172–178.
- [48] B. Tang, J. Yang, Z. Kou, L. Xu, H.L. Seng, Y. Xie, A.D. Handoko, X. Liu, Z.W. Seh, H. Kawai, H. Gong, W. Yang, Surface-engineered cobalt oxide nanowires as multifunctional electrocatalysts for efficient Zn-Air batteries-driven overall water splitting, *Energy Storage Mater.* 23 (2019) 1–7.
- [49] H.R. Hao, Y. Li, Y.Y. Wu, Z. Wang, M.K. Yuan, J.P. Miao, Z. Lv, L.L. Xu, B. Wei, In-situ probing the rapid reconstruction of FeOOH decorated NiMoO₄ nanowires with boosted oxygen evolution activity, *Mater. Today Energy*. (<https://doi.org/10.1016/j.mtener.2021.100887>). (Accepted).
- [50] Z. Xiao, Y. Huang, C. Dong, C. Xie, Z. Liu, S. Du, W. Chen, D. Yan, L. Tao, Z. Shu, G. Zhang, H. Duan, Y. Wang, Y. Zou, R. Chen, S.Y. Wang, Operando identification of the dynamic behavior of oxygen vacancy-rich Co₃O₄ for oxygen evolution reaction, *J. Am. Chem. Soc.* 142 (2020) 12087–12095.
- [51] L. Li, Q. Shao, X.Q. Huang, Amorphous oxide nanostructures for advanced electrocatalysis, *Chem. Eur. J.* 26 (2020) 3943–3960.
- [52] K. Zhu, W. Luo, G. Zhu, J. Wang, Y. Zhu, Z. Zou, W. Huang, Interface-engineered Ni(OH)₂/β-like FeOOH electrocatalysts for highly efficient and stable oxygen evolution reaction, *Chem. Asian J.* 12 (2017) 2720–2726.
- [53] F. Zhang, Y. Shi, T. Xue, J. Zhang, Y. Liang, B. Zhang, In situ electrochemically converting Fe₂O₃-Ni(OH)₂ to NiFe₂O₄-NiOOH: a highly efficient electrocatalyst towards water oxidation, *Sci. China Mater.* 60 (2017) 324–334.